Multi-frequency signatures of space-leader evolution in negative cloud-to-ground lightning stepped leaders

Goldberg, Dylan J.
Nag, Amitabh
Cummins, Kenneth L.
Plaisir, Mathieu N.
Tempert, Alex
Brower, A. Tyler
Biagi, Christopher J.
Brown, Robert G.
Rassoul, Hamid K.

To be published in: Atmospheric Research

DOI to publisher's version: 10.1016/j.atmosres.2026.108835

Multi-frequency signatures of space-leader evolution in negative cloud-to-ground lightning stepped leaders

Dylan J. Goldberg, Amitabh Nag, Kenneth L. Cummins, Mathieu N. Plaisir, Alex Tempert, A. Tyler Brower, Christopher J. Biagi, Robert G. Brown, Hamid K. Rassoul

PII: S0169-8095(26)00099-2

DOI: https://doi.org/10.1016/j.atmosres.2026.108835

Reference: ATMOS 108835

To appear in: *Atmospheric Research*

Received date: 6 September 2025

Revised date: 2 February 2026

Accepted date: 2 February 2026

Please cite this article as: D.J. Goldberg, A. Nag, K.L. Cummins, et al., Multi-frequency signatures of space-leader evolution in negative cloud-to-ground lightning stepped leaders, *Atmospheric Research* (2024), https://doi.org/10.1016/j.atmosres.2026.108835

Multi-Frequency Signatures of Space-Leader Evolution in Negative Cloud-to-Ground Lightning Stepped Leaders

Dylan J. Goldberg[1], Amitabh Nag[1,2], Kenneth L. Cummins[1], Mathieu N. Plaisir[1], Alex Tempert[1], A. Tyler Brower[1], Christopher J. Biagi[3], Robert G. Brown[1], and Hamid K. Rassoul[1]

[1]Florida Institute of Technology, Melbourne, Florida, United States

[2]Los Alamos National Laboratory, Los Alamos, New Mexico, United States

[3]NASA Kennedy Space Center, Florida, United States

Corresponding author: Dylan Goldberg (dgoldberg2018@my.fit.edu)

Abstract

In this study, we examined 364 space leaders in 18 negative natural cloud-to-ground lightning strokes whose stepped leaders created new channels to ground. All strokes were captured on ultra-high-speed video cameras operating at frame rates ranging from 400k to 783k frames per second. Additionally, broadband electromagnetic field measurements were available for a subset of these strokes. The median space leader inception-to-attachment-point length and retrograde propagation speed towards the pre-existing leader channel were 8.2 m and 4.0 x 10^6 m/s, respectively. Space leader lengths were longer and retrograde propagation speeds faster for return strokes with higher peak currents. This is likely due to the relative proximity of space leader inception points to the pre-existing leader channel (PELC), which makes the electric field produced by the PELC line charge density one of the primary factors in determining space leader characteristics. Space leader characteristics were weakly related to their inception altitude. We observed bursts of very high frequency (VHF) emissions preceding, by around 0.5 – 1 μs, electric field leader-step pulses and the visible-frequency-range luminosity pulses started during the step pulses. The median downward leader propagation speed for all 18 strokes was 4.3 x 10^5 m/s; leader propagation speeds were generally faster for return strokes with higher peak currents. Also, leaders appeared to accelerate (on their way to ground) at altitudes lower than about 200 and 1000 m above ground level for strokes in the 10 – 60 and 84 – 228 kA peak current ranges, respectively.

Key Words:

Lightning space leaders, space stems, downward negative stepped leaders, propagation speed, ultra-high-speed video camera measurements, electromagnetic field measurements

1. Introduction

A space leader (SpcL) is a luminous plasma segment that forms in the high electric field region in the vicinity (typically within a few tens of meters) of a negative lightning stepped leader. For SpcLs that attach to the pre-existing leader channel (PELC), the attachment may occur either to the PELC tip leading to its forward extension or to its lateral surface, which may lead to the formation of a new branch (Khounate et al., 2021; Goldberg et al., 2024). Figure 1 shows an example of SpcL evolution from inception to attachment in a negative cloud-to-ground (CG) first stroke. The majority of SpcLs attach to the PELC tip or lateral surface, but some simply disappear without attaching. Detailed characterization of SpcLs is essential for understanding the mechanism of stepping and propagation of negative leaders in natural lightning.

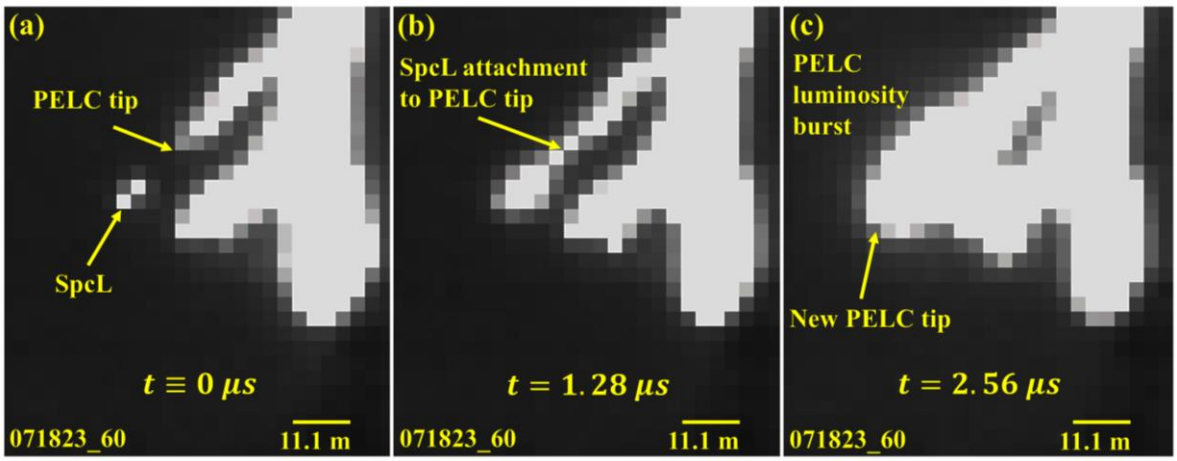

Figure 1. Evolution of an SpcL attaching to a PELC tip in a 60-kA negative CG first stroke occurring at a distance of 5 km, observed in three consecutive ultra-high-speed (UHS) video camera frames. The exposure time for each frame is 740 ns, followed by a deadtime of 540 ns. The resolution of each pixel is 2.8 m. (a) First frame in which SpcL is observed to form ahead of the PELC tip. (b) SpcL attaches to the PELC resulting in the forward extension of the negative leader. (c) Luminosity burst immediately following the SpcL-to-PELC attachment marking the completion of the step formation process. Note that, in order to clearly show the SpcL evolution in this figure, the video camera frames were processed to reduce the brightness of the ambient background; the relative luminosities of the SpcL and the PELC remained unchanged.

Observations of space stems and SpcLs have been reported in the literature over the past decade or so in triggered and natural CG lightning as summarized in Table 1. Note that the terms "space stems" and "space leaders" are sometimes used interchangeably. Probably, space stems evolve into SpcLs once the channel is visibly luminous, indicating significant thermalization. It remains to be seen if space stems in natural lightning leaders would be sufficiently bright to be captured by a camera operating in the visible frequency range. Biagi et al. (2009, 2010) reported high-speed video camera observations of separated luminous segments in triggered lightning that they believed to be space stems or SpcLs. They observed 1 – 4 m long luminous segments forming 1 – 10 m ahead of the leader channels. Hill et al. (2011) observed eight branches of a natural lightning stepped leader recorded at 300k frames per second (fps), with average luminous segment lengths of 3.9 m, located about 2 m ahead of the PELC. Petersen and Beasley (2013) reported high-speed video (10k fps) observations of a natural negative lightning-stepped leader and a subsequent negative dart-stepped leader. They observed high-luminosity segments with lengths ranging from 1 – 5 m which they interpreted as SpcLs. Similarly, Biagi et al. (2014) observed eight luminous segments in a triggered negative stepped leader with high-speed video (108k fps), with lengths ranging from 1 – 6 m, centered at distances between 3 and 8 m from the main negative leader channel. Tran et al. (2014) observed an unusual natural lightning flash with two branched negative strokes to ground with two simultaneous space stems observed during leader descent prior to the first stroke, with step lengths estimated to be 14 – 15 m. Nag and Rakov (2016) showed a conceptual diagram of SpcL formation and attachment to the PELC, and also predicted that leader characteristics would be affected by the different enhanced and reduced electric field regions (due to a lower positive charge region) between the main negative cloud charge region and ground. Qi et al. (2016) reported synchronized electromagnetic field and high-speed video camera observations of a natural negative stepped leader. They found nine field pulses which they attributed to leader steps, and captured a total of 23 SpcLs or space stems with two-dimensional (2-D) lengths ranging from 1 – 13 m, with an arithmetic mean (AM) of 5 m. Their distances from the PELC ranged from 1 – 8 m, with the AM being 4 m. Jiang et al. (2017) reported the characteristics of SpcLs observed in two negative stepped leaders with a video camera frame rate of 180k fps. For 96 leader steps, they found the step lengths to range between 1.3 and 8.6 m, with a geometric mean (GM) of 4.4 m. Additionally, the distances from the center of the SpcL to the PELC ranged from 2.1 – 6.9 m, with the GM being 3.6 m. Srivastava et al. (2019) investigated 34 space stems observed in a negative stepped leader that attached to a 325-m tall tower. The step lengths ranged from 1 – 9 m, with an AM of 4.0 m. Qi et al. (2019) observed 12 SpcLs in 47 steps of a negative stepped leader with high-speed video cameras operating with frame rates of 20k

and 525k fps. They found the step leader lengths to vary between 2 and 5.9 m, with the AM being 3 m. Finally, Khounate et al. (2021) measured the characteristics of SpcLs in three negative stepped leaders using ultra-high-speed (UHS) video cameras with frame exposure times of 1.8, 1.0, and 0.74 μs and reported median 2-D SpcL lengths of 6.1, 16.6, and 17.6 m, respectively. They found that the median SpcL lengths and inception-to-attachment-point distances were longer in higher peak-current return strokes. They inferred that higher stepped-leader line-charge-density in strokes with higher return-stroke peak currents influenced SpcL characteristics.

In this study, we analyze the spatio-temporal evolution of 364 SpcLs occurring in 18 negative stepped leaders in CG strokes that created new channels to ground; this is the largest data set of SpcLs analyzed to date. The peak currents estimated by the U.S. National Lightning Detection Network (NLDN) for the 18 strokes ranged from 10 – 228 kA. These strokes were observed using time-synchronized UHS video camera and electromagnetic field measurements. We examine the impact of SpcL inception-altitude above ground level (AGL) and return stroke peak current on SpcL characteristics.

Table 1. Return stoke-parameters and geometric properties of observed space stems/leaders in rocket-triggered and natural CG lightning observed using high-speed video cameras in different studies.

Study	Number of strokes	Return stroke peak current (kA)	Space stem/leader			Video camera interframe interval (μs)	Observation distance (m)	Lightning type
			Number of space stem/leader	Length (m)	Distance from PELC (m)			
Biagi et al. (2009)	9	-	2	2, 4	4	185, 20	440	Rocket-triggered lightning
Biagi et al. (2010)	5	-	-	1 – 4	1 – 10	4.17	440	
Biagi et al. (2014)	9	-	8	1 – 6	3 – 8	9.26	440	
Hill et al. (2011)	1	-10.6	16	3.9 (AM)	2.1 (AM)	3.33	1000	Natural lightning
Petersen et al. (2013)	1	-35	-	1 – 5	-	100	770	
Tran et al. (2014)	2	-30, -20	2	-	14 – 15	400	6100	
Qi et al. (2016)	1	-	23	5 (AM)	4 (AM)	100, 20	350	
Jiang et al. (2017)	2	-	31	-	3.8 (AM)	5.6	410 – 1030	
Srivastava et al. (2019)	2	-19, -44.3	34	2.1 (AM)	-	2.63	910	
Qi et al. (2019)	2	-13, -28	12	3 (AM)	< 2.7 (AM)	1.9	490	
Khounate et al. (2021)	3	-17 – -228	93	4.3 – 14.4 (AM)	6.2 – 26.5 (AM), 6.1 – 27 (median)	1.26 – 2.5	2700 – 7900	
Present study	18*	-10 – -228	364	10.5 (AM), 8.2 (median)	11.4 (AM), 9 (median)	1.26 – 2.5	400 – 13800	

*Includes SpcLs in three return strokes with peak currents of -17, -104, and -228 kA previously analyzed by Khounate et al. (2021).

2. Measurement Systems, Data, and Methods

We used data from two measurement stations in this study: the Industrial Area Tower (IAT) (Nag et al., 2021, 2023a; Plaisir et al., 2023) at the Kennedy Space Center (KSC) and the Melbourne Lightning Observatory (MLO) (Khounate et al., 2021; Nag et al., 2023b) located on the campus of Florida Institute of Technology. Both measurement stations included electric field, electric field derivative (dE/dt), magnetic field derivative (dB/dt), and VHF measurement systems. The electric field and dE/dt systems had –3 dB bandwidths of 0.16 Hz – 12 MHz and near-DC – 13 MHz, respectively. The VHF system's passband gain was about 24 – 26 dB and the -3 dB and -6 dB bandwidths were 16 – 215 and 15.6 – 410 MHz, respectively. Data from all measurement systems, except the VHF, were transmitted from the antenna and associated electronics via fiber optic links to digitizers operating at 100 MHz sampling rate. For the VHF measurement system, low loss double-shielded coaxial cables were used to transmit the data to a digitizer sampling at 1.25 GHz. At each measurement station, a UHS video camera recorded lightning at frame rates ranging from 400k to 783k fps. Note that, the KSC IAT is instrumented with a current measurement system installed at the top of the tower designed to measure the currents of upward unconnected and connecting leaders as well as return strokes attaching to the tower (Nag et al., 2021, 2023; Plaisir et al., 2023); however, we do not analyze any current waveform data in this study which is focused on the downward stepped leaders of 18 strokes (8 and 10 strokes observed at the KSC IAT and MLO, respectively). We used the NLDN-estimated peak currents for all strokes (including the ones for which we had channel-base current measurements) for consistency; they ranged from -10 to -228 kA. Differences in the measured and NLDN-estimated peak currents were small and will be the subject of a later study. For three strokes (all at the MLO), we simultaneously recorded UHS video camera, electric and/or magnetic field, and VHF measurements, and for 15 strokes (at the MLO and KSC IAT) we acquired UHS video camera measurements only. For the three strokes with simultaneously measured UHS video camera and electromagnetic field measurements, the field measurements were triggered using the trigger-pulse generated by the image-based auto trigger of the UHS video camera when it sensed light exceeding a pre-set threshold within its field of view. We time-aligned the different measurement channels taking into account all cable delays for all systems as well as the speed-of-light propagation delay between the lightning location (the NLDN-reported 2-D ground-strike-point locations for the three strokes) and our sensors. All data were GPS time-stamped with an accuracy of 10 ns.

Table 2. Characteristics of strokes, derived from NLDN-reports and video camera parameters, observed at the KSC IAT and MLO.

Location	Number of strokes	Number of SpcLs	NLDN-reports		Interframe interval (µs)	Video camera characteristics				
			Return stroke peak current magnitude (kA)	Distance to stroke (km)		Frame exposure time (µs)	Dead time (µs)	Frame size, H x V (pixels)	Pixel resolution (m/pixel)	Altitude range AGL of field of view (m)
KSC IAT	8	170	13 – 97	0.4 – 1.8*	1.26 – 1.28	0.74	0.52 – 0.54	64 x 128	0.78 – 3.62	41 – 646
MLO	10	194	10 – 228	1.1 – 13.7*	1.26 – 2.5	0.74 – 1.80	0.52 – 0.70	64 x 128, 128 x 64	0.91 – 7.71	18 – 1399

*The distance to stroke from camera for the five strokes that attached to the KSC IAT was 752 m and for the stroke that attached to a tower within the field of view of the video camera at the MLO was 1.9 km. These distances were used for determining the pixel resolution. The NLDN-reported distances are provided here for completeness.

A total of 364 SpcLs were identified during the stepped leaders of 18 negative CG strokes that created new channels to ground. The number of return strokes and SpcLs, as well as the NLDN-reported characteristics and video camera parameter ranges for observations at the KSC IAT and MLO are shown in Table 2. Five of the eight strokes observed (occurring within the field of view of the video camera) at the KSC IAT measurement station attached to the tower. Only one of the 10 strokes recorded at the MLO attached to a nearby tower within the camera's field of view. For the six strokes that attached to the two towers, we used the location of the towers as the ground-strike-point location; for the other 12 strokes we used the NLDN-reported ground-strike-point locations. One of the strokes that attached to the KSC IAT (stroke 080823_21) was a second stroke whose downward leader deviated from the first-stroke (stroke 080823_36) leader channel and progressed in a stepwise fashion to attach to a new upward connecting leader initiated from the KSC IAT; we included in our dataset the 24 SpcLs associated with the downward leader stepping of this second stroke. For all strokes, we calculated the 2-D distances from our UHS cameras to the ground-strike-point locations which were either the locations of the towers (KSC IAT or the one near the MLO) or NLDN-reported stroke locations. Then for each stroke, we used this distance, along with the respective UHS video cameras' parameters (lens focal length and pixel size), to calculate the pixel resolution on the 2-D plane of the camera's field of view. The vertical field of view of our UHS video cameras varied with frame rate and distance to stroke; the maximum and minimum altitudes AGL were 1399 and 18 m, respectively. The UHS video cameras' pixel resolution, calculated from the return-stroke location and UHS video camera parameters, ranged from 0.78 – 7.71

m/pixel. The pixel resolution error for each stroke was calculated by finding the maximum distance from the camera that the return stroke could have occurred (within the camera's field of view), given the NLDN-reported 50% error ellipse axes lengths and orientation/angle. For the 12 strokes that didn't attach to towers, the pixel resolution error ranged from 0.11 – 0.40 m/pixel, with the median error being 0.11 m/pixel. For the six strokes that attached to towers in our cameras' fields of view, the pixel resolution error is zero because the exact ground strike point location is known. Note that all lightning channel-lengths estimated from our video camera records in this study were 2-D and may be underestimates of their 3-D lengths by up to 30% (Gao et al., 2014; Idone et al., 1984).

We used the same methodology for identifying SpcLs as Khounate et al. (2021) who considered a luminous segment to be an SpcL if it was first observed to be visually separated in a video camera frame by one or more pixels from the PELC. The distance between each SpcL and its PELC-tip/attachment point was measured between the mid-point of the SpcL (camera pixel or group of pixels illuminated by the SpcL) and the PELC-tip/attachment point. Additionally, we did not distinguish between space "stems" and space "leaders" as once the channel is visibly luminous, indicating significant thermalization, it should probably be referred to as a "leader". We do not know if space stems in natural lightning leaders would be sufficiently bright to be captured by a camera operating in the visible frequency range.

3. Analysis and Results

3.1 Video camera-derived characteristics of space leaders

We found the 2-D positions of SpcL inception-points with respect to the PELC for all 364 observed SpcLs in the 18 strokes in our dataset. Figure 2a shows the inception point of each SpcL that later attached to the tip (red dot) or the lateral surface (green dot) of the PELC or remained unattached (blue dot). The black line in the figure indicates the reference-line along which the PELC associated with each observed SpcL was aligned, with its tip located at the center of the polar plot. The 2-D position of each SpcL on the plane of the plot was then determined by measuring the length of the line joining the inception point of the SpcL and the PELC tip (i.e., the inception point to PELC tip distance) as well as the angle between this line and the PELC-reference-line. As an example, the 2-D distance and angle between PELC and SpcL are shown in the video camera frame in Figure 2c. From Figure 2a, we see that 272 of 273 (99.6%) SpcLs that attached to the PELC tip formed in the region below or ahead of the PELC tip (i.e.,

below the 90 – 270° line; the SpcL was closer to ground than the PELC tip). Only one such SpcL formed above the PELC tip (i.e., above the 90 – 270° line; the PELC tip was closer to ground than the SpcL). On the other hand, most (32 of 53 or 60.4%) of the SpcLs that attached to the PELC lateral surface formed above the leader tip. Also, the majority (28 of 38 or 73.7%) of SpcLs that remained unattached originated below the PELC tip. The statistics of the SpcL inception-point to PELC-tip distance for all 364 SpcLs in the 18 negative strokes are shown in the table in Figure 2b. The median distances to the PELC-tip of SpcLs that attached to the tip (N = 273) and lateral surface (N = 53) were 8.1 and 11.2 m, respectively, and that for SpcLs that remained unattached (N = 38) was 12.9 m.

(a)

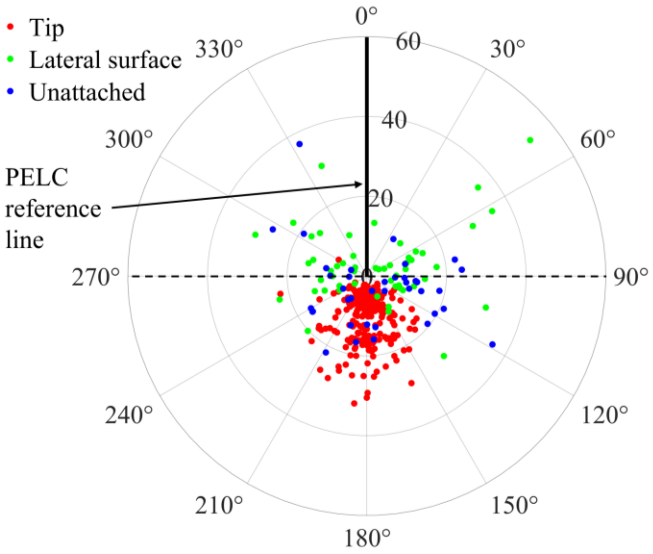

(b)

Attachment type	Tip	Lateral surface	Unattached	All
N	273	53	38	364
AM (m)	10.4	14.1	14.4	11.4
SD (m)	6.2	10.1	7.9	7.2
SE (m)	0.4	1.4	1.3	0.4
Median (m)	8.1	11.2	12.9	9.0
GM (m)	8.9	11.3	12.4	9.5
Min (m)	2.2	3.0	3.9	2.2
Max (m)	32.1	53.3	37.1	53.3

(c)

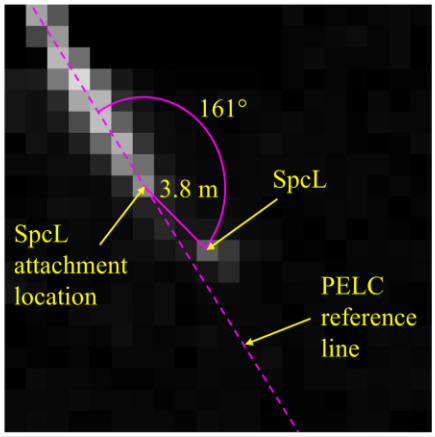

Figure 2. (a) Polar plot showing locations of SpcLs relative to the PELC tip at the time of their inception on a 2-D plane. The black vertical line indicates the reference-line along which the PELC associated with each observed SpcL was aligned, with its tip located at the center of the plot. The radii of the gray circles indicate distances of 20, 40, and 60 m from the PELC tip. The 90 – 270° line, shown by the horizontal dashed line, separates the regions below and above the PELC-tip. The SpcLs are color-coded based on

their attachment location on the PELC. (b) Table showing the statistics for the SpcL inception-point distances from the PELC tip, including sample size (N), AM, standard deviation (SD), standard error (SE) of the mean, median, GM, minimum (Min), and maximum (Max). (c) A video camera frame showing, as an example, the 2-D distance and angle between a PELC and an SpcL. The pixel resolution for this frame was 0.78 m/pixel.

In Figure 3a, we show the histogram of the maximum SpcL length, which is defined as the distance between its inception point to its attachment point on the PELC, color coded by attachment location on the PELC. The associated statistics are shown in the table in Figure 3b. Note that the lengths of the 38 SpcLs that did not attach to the PELC are not included in this analysis. Additionally, we do not observe (perhaps due to the limited spatio-temporal resolution of our video camera records) any clear indication of bidirectional leader development for our SpcLs during their evolution prior to their attachment to the PELC (see Section 4 for further discussion). Therefore, we define the maximum SpcL length to be equal to the distance between its inception point to its attachment point on the PELC. The AM, median, and GM of the maximum SpcL length for 273 tip-attachment versus 53 lateral-surface-attachment SpcLs were comparable, with the median length for 326 SpcLs in 18 strokes being 8.2 m. Note that our measurements of SpcL inception-to-attachment-point lengths were affected by the pixel resolution of our UHS video camera records which ranged from 0.78 – 7.71 m/pixel. For video camera records with longer length/pixel, we expect that shorter SpcL inception-to-attachment-point lengths were not measurable, so, the average lengths shown in Figure 3b should be treated as underestimates. Note that the pixel associated with the inception point of an SpcL remains illuminated throughout the progression of the SpcL from inception point to PELC-attachment; this makes it clear that the frame dead time does not have a large impact on our measurements of SpcL length.

Next, we found the time it took an SpcL to attach to the PELC after forming by calculating the time difference between the first video camera frame in which we observed the SpcL and the first frame in which we saw it attached to the PELC. Figure 4a shows a histogram of these times for 326 SpcLs, color coded by attachment location on the PELC. For both, the 273 SpcLs that attached to the PELC tip and the 53 SpcLs that attached to the PELC lateral surface, the median time was 2.5 μs. The AM (± SE) for the two types of SpcLs were 2.8 (± 0.1) and 3.6 (± 0.4) μs, respectively. Note that, our measurement of the SpcL time-to-attachment was limited by our camera interframe intervals (exposure time plus dead time in Table 2) which ranged from 1.26 – 2.5 μs. The median time-to-attachment of 2.5 μs as well as the other averages shown in Figure 4b should, therefore, be treated as overestimates. Also, the discrete nature of the interframe intervals of 1.26 and 2.5 μs resulted in no values falling in the 4.0 – 5.0 μs and

9.0 – 10 µs bins in Figure 4a. For 282 SpcLs that were captured with a frame rate of 1.26 or 1.28 µs, the AM and median time-to-attachment were 2.8 and 2.5 µs, respectively.

(a)

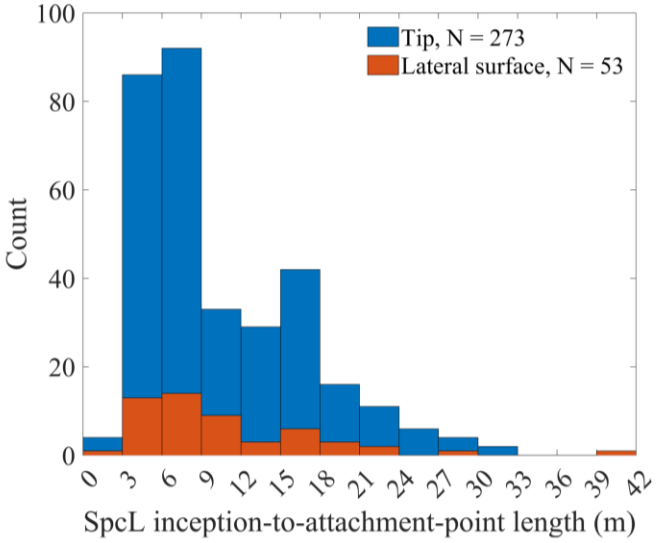

(b)

Attachment type	Tip	Lateral surface	All
N	273	53	326
AM (m)	10.4	10.8	10.5
SD (m)	6.2	7.2	6.4
SE (m)	0.4	1.0	0.4
Median (m)	8.1	8.7	8.2
GM (m)	8.9	9.0	8.9
Min (m)	2.2	2.9	2.2
Max (m)	32.1	40.7	40.7

Figure 3. (a) Histogram of SpcL inception-to-attachment-point lengths for SpcLs that attached to their PELC, grouped by tip attachment (blue) and lateral surface attachment (orange). (b) Table showing the statistics for the SpcL inception-to-attachment-point lengths.

(a)

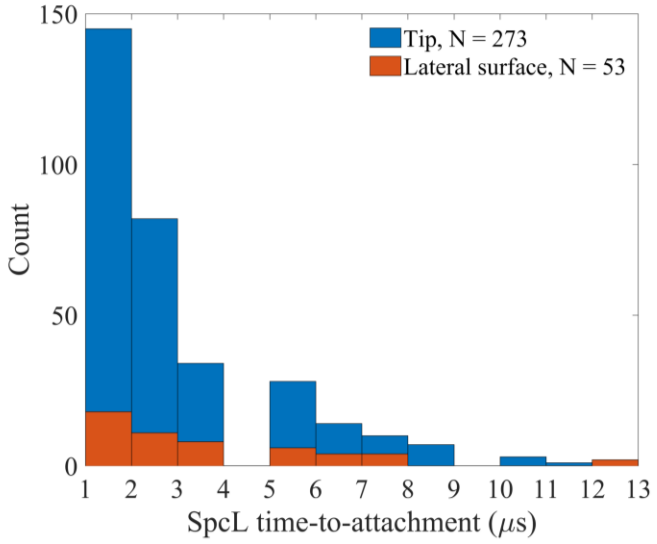

(b)

Attachment type	Tip	Lateral surface	All
N	273	53	326
AM (µs)	2.8	3.6	2.9
SD (µs)	2.1	2.7	2.2
SE (µs)	0.1	0.4	0.1
Median (µs)	2.5	2.5	2.5
GM (µs)	2.3	2.9	2.3
Min (µs)	1.3	1.3	1.3
Max (µs)	11.9	12.6	12.6

Figure 4. (a) Histogram of time-to-attachment for SpcLs that attached to their PELC, grouped by tip attachment (blue) and lateral surface attachment (orange). (b) Table showing the statistics for the SpcL time-to-attachment. Note that our frame durations of 1.26, 1.28, 1.7, and 2.5 µs resulted in no durations

being reported between 4 and 5 μs. This is apparent in the histogram where there are no times reported for the 4 – 5 μs bin.

For SpcLs that attached to the PELC, we also examined the SpcL retrograde propagation speed, i.e., its propagation speed toward the PELC obtained by dividing the maximum SpcL length (see Figure 3) by the SpcL formation to PELC attachment time (see Figure 4). Figure 5a shows a histogram of SpcL propagation speeds color coded by attachment location on the PELC. Overall, the median propagation speed for the 326 SpcLs in 18 strokes was 4.0 x 10^6 m/s (see Figure 5b). For SpcLs that attached to the PELC tip (N = 273) versus the lateral surface (N = 53), the median retrograde propagation speeds were 4.1 x 10^6 and 3.0 x 10^6 m/s, respectively. Since, on average, the SpcL lengths are underestimated and times-to-attachment overestimated, we expect the average retrograde propagation speeds shown in Figure 5b to be underestimated.

(a)

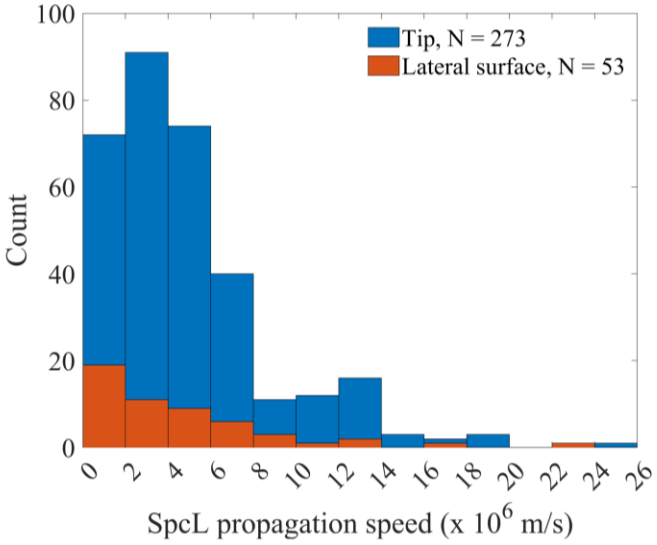

(b)

Attachment type	Tip	Lateral surface	All
N	273	53	326
AM (x 10^6 m/s)	5.0	4.6	5.0
SD (x 10^6 m/s)	3.9	4.5	4.0
SE (x 10^6 m/s)	0.2	0.6	0.2
Median (x 10^6 m/s)	4.1	3.0	4.0
GM (x 10^6 m/s)	3.9	3.1	3.8
Min (x 10^6 m/s)	0.7	0.4	0.4
Max (x 10^6 m/s)	25.5	24.0	25.5

Figure 5. (a) Histogram of SpcL propagation speeds color coded by attachment type. The blue and orange color coding represents SpcLs that attached to the PELC tip and lateral surface, respectively. (b) Table showing the statistics for SpcL propagation speeds.

3.2 Impact of altitude and return stroke peak current on space leader characteristics

We first examined the impact of the return stroke peak current on SpcL characteristics. Figure 6 shows SpcL inception-to-attachment-point lengths binned by four different return stroke peak current

ranges: 10 – 17 kA (blue), 18 – 30 kA (orange), 36 – 60 kA (yellow), and 84 – 228 kA (purple). These ranges included 5, 6, 3, and 4 strokes, respectively, and 90, 58, 60, and 118 SpcLs, respectively. The median inception-to-attachment-point lengths were 6.1, 5.5, 8.2, and 16.6 m, respectively. We see that strokes with higher peak currents generally had longer SpcL inception-to-attachment-point lengths than strokes with lower peak currents.

(a)

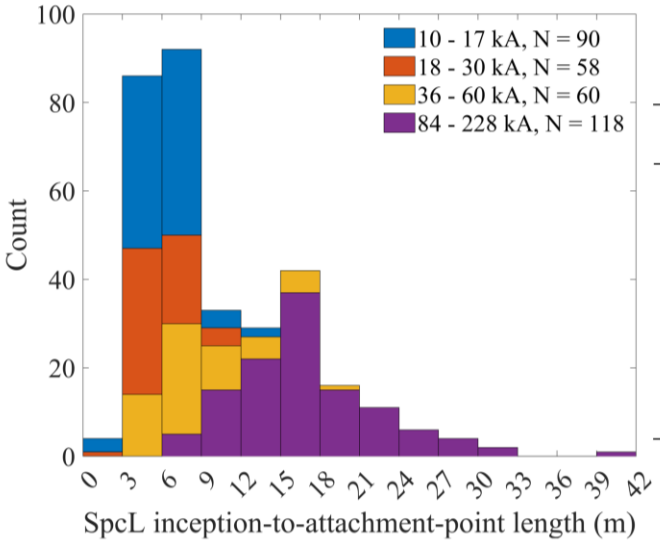

(b)

Peak current range	10 – 17 kA	18 – 30 kA	36 – 60 kA	84 – 228 kA	All
N	90	58	60	118	326
AM (m)	6.2	5.9	8.7	17.0	10.5
SD (m)	2.0	2.0	4.0	5.6	6.4
SE (m)	0.2	0.3	0.5	0.5	0.4
Median (m)	6.1	5.5	8.2	16.6	8.2
GM (m)	5.9	5.6	7.9	16.2	8.9
Min (m)	2.4	2.2	3.0	7.8	2.2
Max (m)	14.5	11.0	18.6	40.7	40.7

Figure 6. (a) Histogram and (b) statistics of SpcL inception-to-attachment-point lengths grouped by different return stroke peak current ranges.

(a)

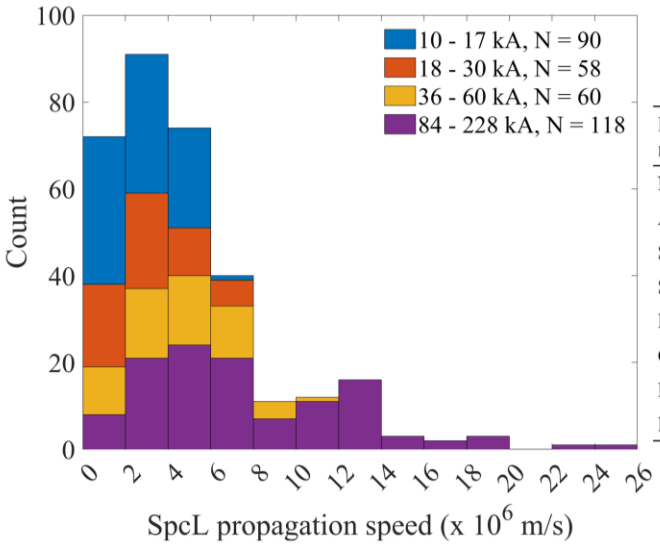

(b)

Peak current range	10 – 17 kA	18 – 30 kA	36 – 60 kA	84 – 228 kA	All
N	90	58	60	118	326
AM (x 10^6 m/s)	2.9	3.2	4.4	7.7	5.0
SD (x 10^6 m/s)	1.5	1.7	2.4	5.0	4.0
SE (x 10^6 m/s)	0.2	0.2	0.3	0.5	0.2
Median (x 10^6 m/s)	2.5	2.7	4.5	6.7	4.0
GM (x 10^6 m/s)	2.5	2.8	3.7	6.2	3.8
Min (x 10^6 m/s)	0.4	0.7	0.6	1.3	0.4
Max (x 10^6 m/s)	6.1	7.2	11.2	25.5	25.5

Figure 7. (a) Histogram and (b) statistics of SpcL retrograde propagation speeds grouped by different return stroke peak current ranges.

Figure 7 shows the SpcL retrograde propagation speeds grouped by the same return stroke peak current ranges used in Figure 6. The median SpcL propagation speeds for the four peak current ranges (in order of increasing current) were 2.5 x 10^6, 2.7 x 10^6, 4.5 x 10^6, and 6.7 x 10^6 m/s. SpcLs in strokes with higher peak currents appeared to propagate faster from their inception locations to the PELC than SpcLs in strokes with lower peak currents.

To determine the dependence of the SpcL inception-to-attachment-point length (L_{SL}) on both the inception altitude (h) and return stroke peak current (I), we plotted a surface described by a power-law relationship between the three parameters given by:

$$L_{SL} = a * I^b * h^c \quad (1)$$

where a, b, and c are constants determined for the best fitted surface. A power law relationship was chosen to account for any non-linearities (geometric increase, decrease, or compression) in the relationships between parameters, and separate constants for peak current and height (b and c, respectively) were used so that the impact of high and low peak currents and altitudes could be examined independently. Figure 8a shows the surface fit for all 326 SpcLs that attached to the PELC. The coefficient of determination (R^2) was 0.68. We also examined the relationship between the SpcL lengths separately versus return stroke peak currents and inception altitudes (by setting c = 0 and b = 0, respectively, in Equation 1), as shown in Figures 8b and 8c, respectively. The parameters used in Equation (1) to plot each power-law fit are shown in the table in Figure 8e. The R^2 value was higher (0.68), and the sum of squared errors (SSE) was lower (4141) for SpcL length versus return stroke peak current (Figure 8b) compared to those (0.20 and 10428, respectively) for SpcL length versus inception altitude (Figure 8c). This indicated a stronger dependence of SpcL length on the return stroke peak current than on inception altitude. Figure 8d shows the AM (blue hollow circles) ± SE (blue lines) and median (red dots) SpcL lengths versus return stroke peak current for our 18 strokes; a significant increase in AM/median SpcL length for strokes with peak currents higher than about 45 kA can be observed in the plot. Similarly, we used the following equation

$$S_{SL} = a * I^b * h^c \quad (2)$$

to determine the dependence of the SpcL propagation speed (S_{SL}) on the inception altitude and return stroke peak current. The resulting power-law fit surface is shown in Figure 9a; the R^2 value was 0.51. The

R^2 values associated with SpcL propagation speed versus current and SpcL propagation speed versus altitude were 0.52 (Figure 9b) and 0.44 (Figure 9c), respectively. This indicated a slightly stronger dependence of SpcL propagation speed on return stroke peak current than on altitude, but both parameters are relevant. Figure 9d shows the AM (blue circle) ± SE (blue lines) and median (red dot) SpcL lengths versus return stroke peak current for our 18 strokes; the AM/median SpcL propagation speed increased somewhat for strokes with peak current higher than about 60 kA.

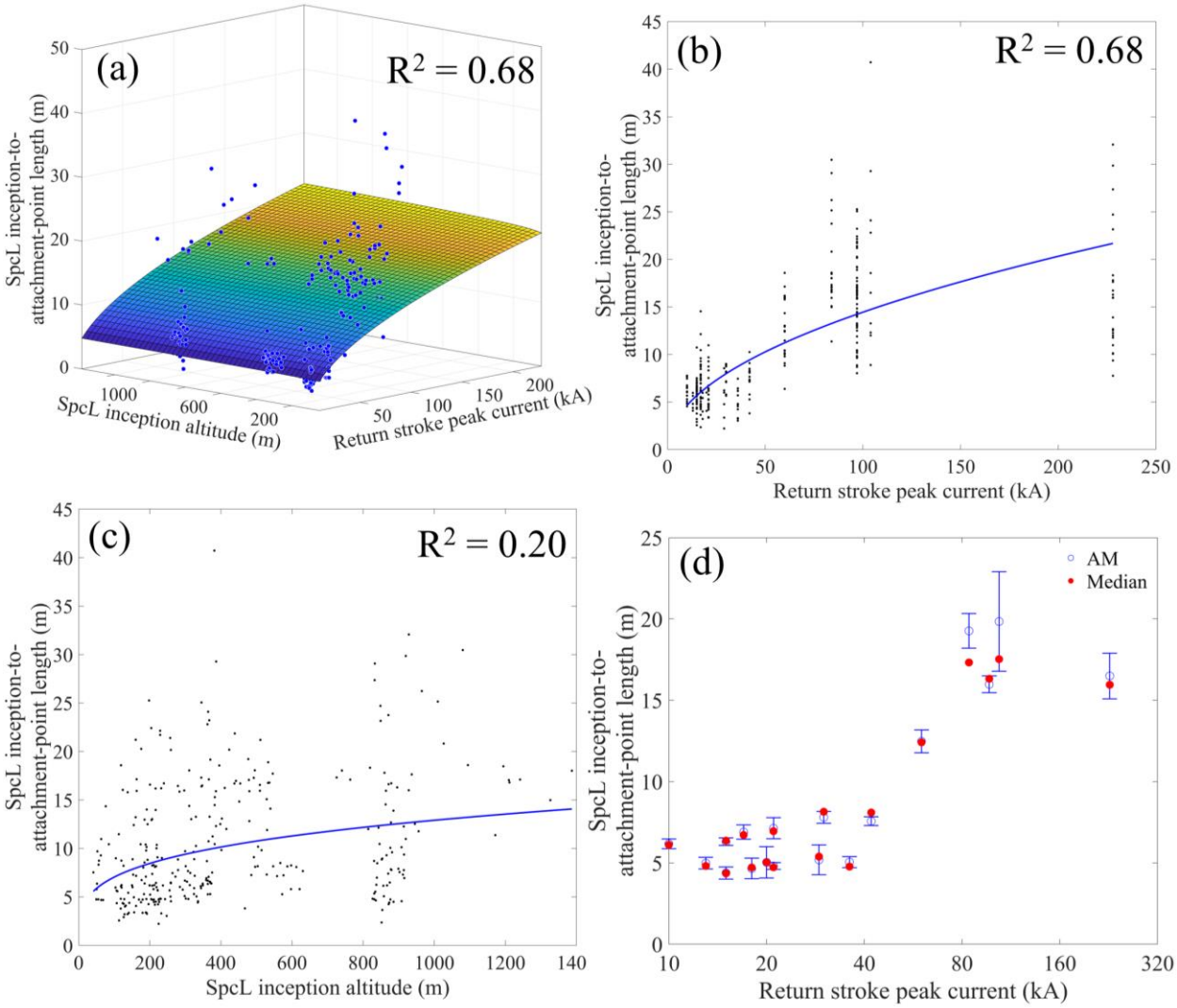

(e)

Graph	a	b	c	R^2	SSE	N
Surface fit (see (a))	1.4	0.5	0.02	0.68	4155	326
Just I (see (b))	1.5	0.5	0	0.68	4141	326
Just h (see (c))	2.1	0	0.3	0.20	10428	326

Figure 8. Dependence of the SpcL inception-to-attachment-point length on return stroke peak current (*I*) and the inception altitude (*h*) for 326 SpcLs in our dataset examined using the power-law relationship shown in Equation 1. (a) Surface fit describing SpcL inception-to-attachment-point length as a function of SpcL inception altitude and return stroke peak current. (b) Scatter plot of SpcL inception-to-attachment-point length and return stroke peak current. (c) Scatter plot of SpcL inception-to-attachment-point length and inception altitude. (d) Scatter plot showing the AM (blue hollow circles) and median (red dots) SpcL inception-to-attachment-point length versus the return stroke peak current for 18 strokes. The blue lines (error bars) centered on the blue circles indicate the range of SEs of the respective AMs. Note that, in (d), the horizontal axis (peak current) is non-linear. (e) Values of the constants in Equation 1 used to obtain the best fits shown in (a), (b), and (c) as well as the parameters (coefficient of determination or R^2, sum of squared errors or SSE and sample size or N) of the best fits.

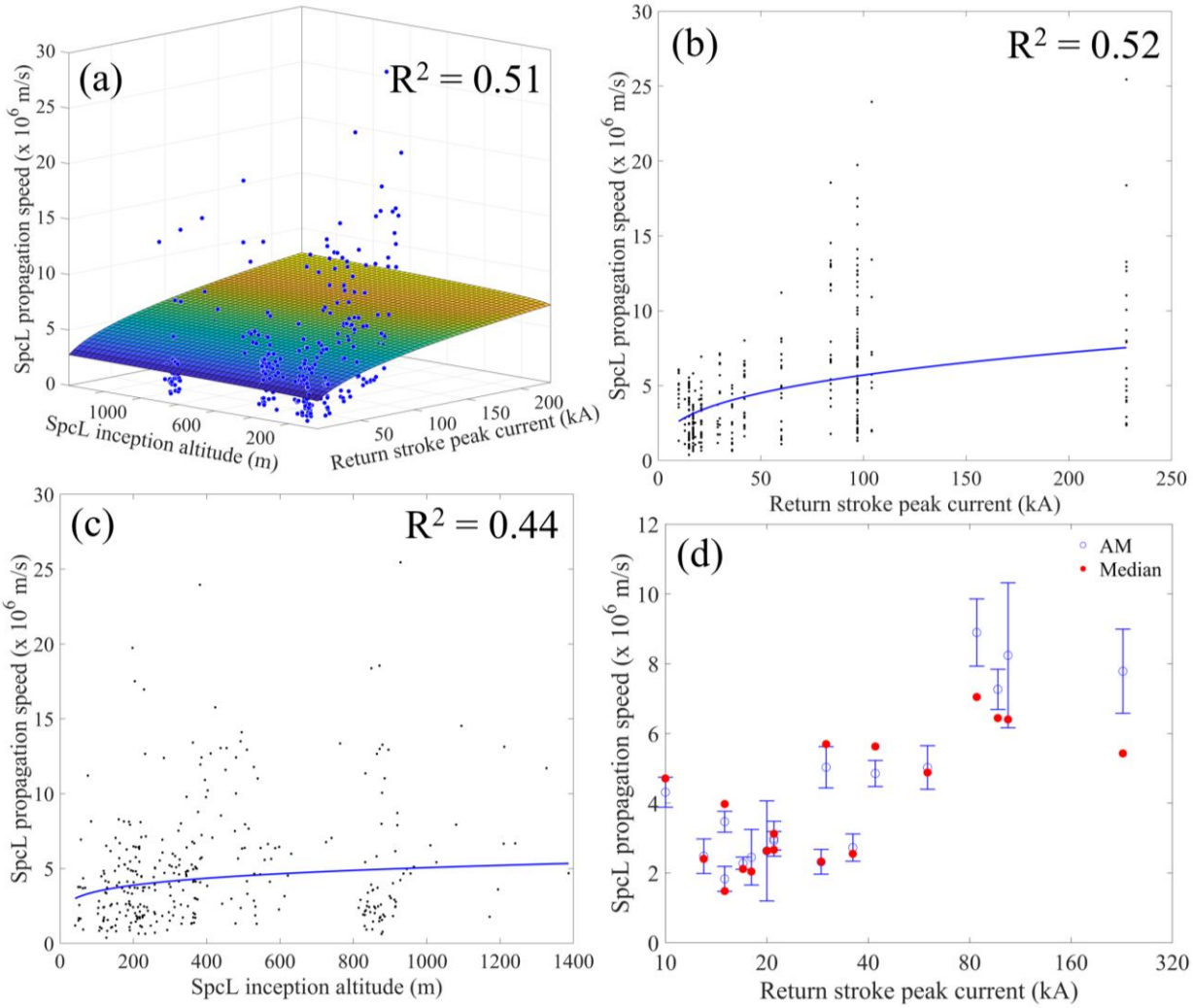

(e)

Graph	a	b	c	R^2	SSE	N
Surface fit (see (a))	1.0	0.3	0.03	0.51	2489	326
Just I (see (b))	1.2	0.3	0	0.52	2451	326
Just h (see (c))	1.6	0	0.2	0.44	2857	326

Figure 9. Same as Figure 8 plots but for SpcL retrograde propagation speed versus inception altitude and return stroke peak current. (a) Surface fit describing SpcL speed as a function of SpcL inception altitude and return stroke peak current. (b) Scatter plot of SpcL speed and return stroke peak current. (c) Scatter plot of SpcL speed and inception altitude. (d) Scatter plot showing the AM (blue hollow circles) and median (red dots) SpcL speed versus the return stroke peak current for 18 strokes. The blue lines (error bars) centered on the blue circles indicate the range of SEs of the respective AMs. Note that, in (d), the horizontal axis (peak current) is non-linear. (e) Values of the constants in Equation 2 used to obtain the best fits shown in (a), (b), and (c) as well as the parameters (coefficient of determination or R^2, sum of squared errors or SSE and sample size or N) of the best fits.

3.3 Correlated optical and electromagnetic field emissions from space leaders

In Figure 10 we show the time-correlated broadband electric field, dE/dt, VHF, and video camera data for three SpcLs shown on a 35-μs time-window in one of our stepped leaders (stroke 071823_60). The NLDN reported return stroke peak current for this stroke was -60 kA. Figure 10b shows the measured dE/dt waveform (left vertical axis, blue line) along with the mean gray level calculated from the entire field-of-view of the video camera frames (right vertical axis, orange line), Figure 10c shows the electric field obtained by integrating the dE/dt, Figure 10d shows the VHF emissions, and Figure 10e shows the time-frequency spectrogram of the VHF emissions in the 125 – 300 MHz range. Three distinct dE/dt pulses are labeled as (1), (2), and (3) (above Figure 10b) corresponding to the three optically observed SpcLs; three consecutive video camera frames for each of the three SpcLs are shown in Figure 10a. Each frame has an exposure time of 740 ns followed by a deadtime of 540 ns. For each SpcL, the first frames (left-most column) show the SpcL forming ahead of the leader channel, and the next two frames show the SpcL's progression toward and attachment to the leader channel followed by channel rebrightening. The vertical black dashed lines in Figures 10b-e indicate the peak times of the electric field signatures of what are traditionally called leader step pulses. We observe that the peaks in the electric field pulses precede the mean gray level luminosity peaks and correspond to the time when the SpcLs appear to attach to the PELC, after which the luminosity pulses start to rise toward their peak. Note that at least a portion of the delay of the optical pulse peaks relative to the electric field pulse peaks could be due to the slower sampling rate (video camera interframe interval) of the mean gray level waveform. The luminosity peaks are associated with channel heating associated with current "propagating" back along the PELC after the SpcL attached to the PELC. Also, we observe from Figures 10d and 10e that there is a burst of VHF emissions near the start of each dE/dt step pulse. See Section 4 for further discussion. The observations for stroke 071823_60 described above are representative of those for all three of our strokes with simultaneously recorded dE/dt, VHF, and UHS video.

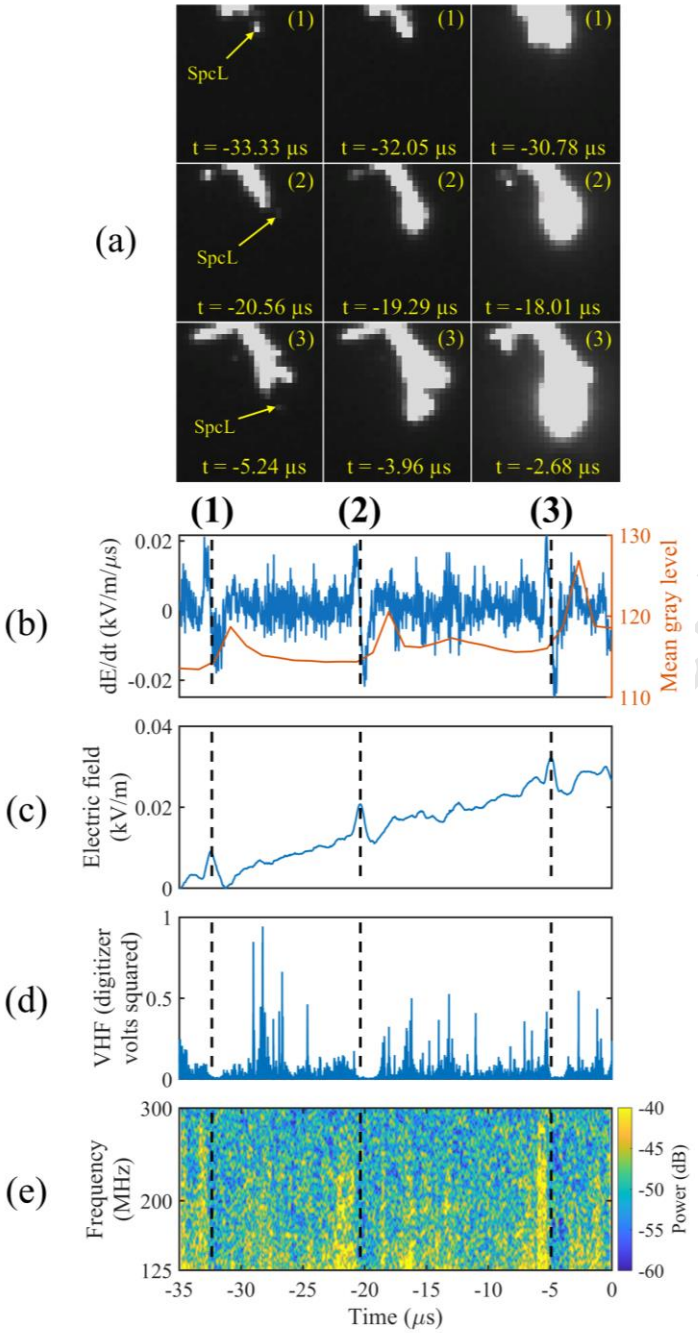

Figure 10. Time-correlated dE/dt, electric field, and VHF measurements along with UHS video camera frames corresponding to three SpcLs labelled (1), (2), and (3) that attached to the PELC for a -60 kA first stroke (stroke 071823_60). (a) Three consecutive UHS video camera frames each for SpcLs labelled (1), (2), and (3). The field of view (range of 2-D spatial locations) shown in all nine frames are identical. Plots of (b) dE/dt (blue line, left vertical axis) and video camera frame mean gray level (orange line, right vertical axis), (c) electric field, and (d) predominantly VHF (16 – 215 MHz) signatures shown on a 35 µs time scale.

(e) The time-frequency spectrogram of the VHF signature shown in (d) for the 125 – 300 MHz range. The vertical black dashed lines in (b) – (e) indicate the peak-times of the leader-step electric field pulses.

3.4 Downward leader propagation speeds

We calculated the downward leader propagation speeds for all 18 strokes from our UHS video camera records. The tip of the downward-leader branch that eventually attached to ground was first identified and the progression of the tip was tracked in all video camera frames between when it entered and exited our camera's field of view. However, for two of our strokes (091924_10 and 091924_15), the downward-leader branch that eventually attached to ground was outside the camera's field of view. For these two strokes, the tip of the downward-leader branch that occurred within the camera's field of view and progressed closest to ground at the time of the return stroke was tracked. For all strokes, the leader propagation speed was calculated as the ratio of the tip-progression distance and the time interval between frames in which the downward-leader tip was observed to advance by more than one pixel. Figure 11 shows a histogram and table of associated statistics for 340 measurements of the downward leader propagation speed for the 18 strokes, categorized into four different peak current ranges (same ranges as those in Figures 6a and 7a). The median downward leader propagation speeds for the 10 – 17 kA, 18 – 30 kA, 36 – 60 kA, and 84 – 228 kA peak current ranges were 2.8×10^5, 4.0×10^5, 5.2×10^5, and 8.1×10^5 m/s, respectively. The median downward leader propagation speed increased with increasing return stroke peak current; for all strokes combined it was 4.3×10^5 m/s. In Figure 12, we show the median downward leader propagation speed versus median altitude for strokes in the 10 – 17 kA, 18 – 30 kA, 36 – 60 kA, and 84 – 228 kA peak current ranges indicated by blue, orange, yellow, and purple lines, respectively. In order to obtain the median line plots, first, the propagation speeds and the corresponding altitudes for the 18 strokes were sorted by descending altitude. Then, the sorted data were binned into eight groups each containing nearly equal number of data points and the median altitude and speeds were computed for each bin. Additionally, in Figure 12, we indicate the AM (± SE) and median speeds using hollow circles (along with whiskers) and solid dots, respectively, for all 14 strokes in the 10 – 60 kA range plotted versus the median altitudes. For the strokes in the 10 – 60 kA range, we see that below about 200 m AGL, the leader propagation speed increases. For the 84 – 228 kA peak current range (purple line), our observations did not include any downward leaders propagating below about 200 m AGL. For strokes in this higher peak current range the downward leader propagation speed started to generally increase at a higher altitude, below around 1000 m AGL.

(a)

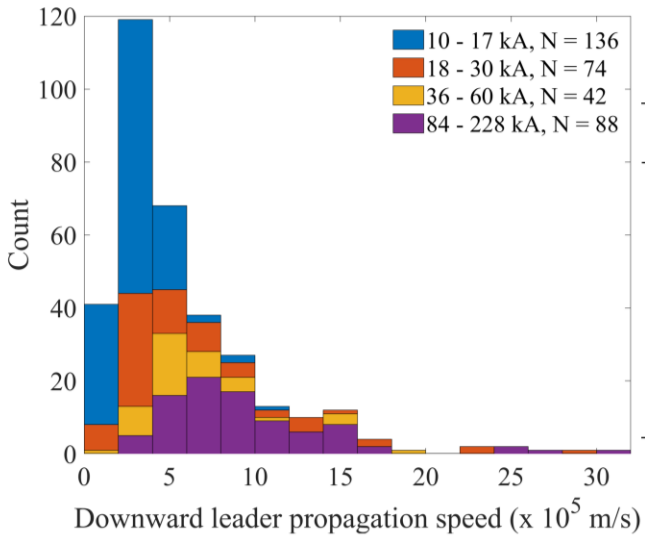

(b)

Peak current range	10 – 17 kA	18 – 30 kA	36 – 60 kA	84 – 228 kA	All
N	136	74	42	88	340
AM (x 10^5 m/s)	3.1	6.0	6.4	9.4	5.8
SD (x 10^5 m/s)	1.6	5.4	3.8	5.2	4.7
SE (x 10^5 m/s)	0.1	0.6	0.6	0.6	0.3
Median (x 10^5 m/s)	2.8	4.0	5.2	8.1	4.3
GM (x 10^5 m/s)	2.7	4.5	5.6	8.3	4.4
Min (x 10^5 m/s)	0.5	0.9	1.7	2.2	0.5
Max (x 10^5 m/s)	10.5	28.2	19.0	31.7	31.7

Figure 11. (a) Histogram of downward leader propagation speeds calculated from UHS video camera frames for all 18 strokes. (b) Statistics associated with downward leader propagation speed histogram.

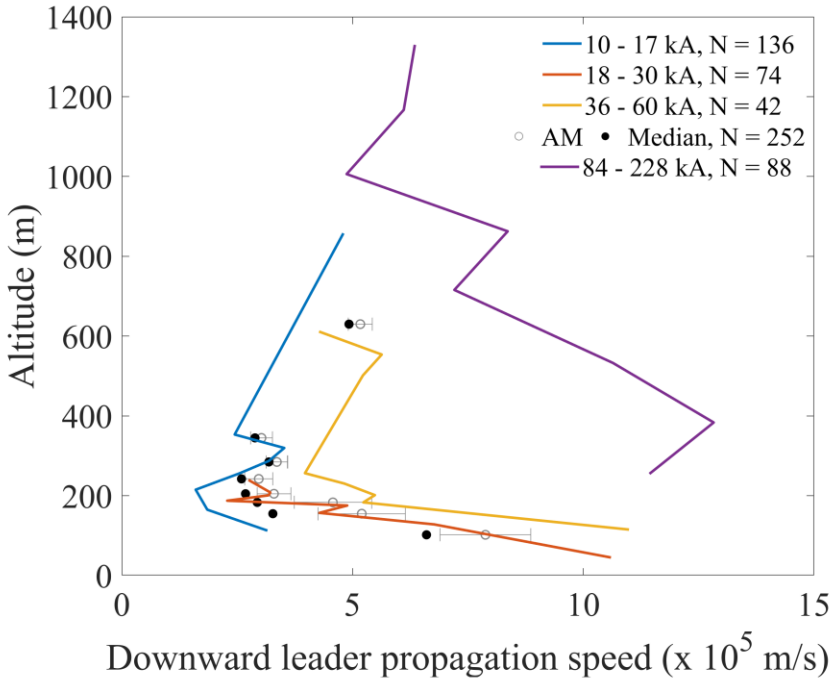

Figure 12. Median downward leader propagation speed versus median altitude for strokes in the 10 – 17 kA, 18 – 30 kA, 36 – 60 kA, and 84 – 228 kA peak current ranges indicated by blue, orange, yellow, and purple lines, respectively. Also shown are the AM (± SE) and median speeds using hollow circles (along with whiskers) and solid dots, respectively, for all strokes in the 10 – 60 kA range plotted versus the median altitudes. Note that, the AMs and SEs are different than those that appear in Figure 11b because the data here is binned by decreasing median altitude instead of by peak current range.

4. Discussion

We did not observe any clear indication of significant bidirectional propagation in our SpcLs prior to their attachment to the PELC; only the positively charged ends of the SpcLs (the ends closer to the PELC-tip) were observed to propagate toward the negatively charged PELC-tip while the negatively charged SpcL ends (far ends of the SpcLs relative to the PELC-tip) remained more-or-less in the same location. Note that, in Figures 1 and 10a, we observe that once the SpcLs have attached to the PELC, additional pixels below the inception point of the SpcLs have been illuminated. This could be due to saturation of the nearby pixels associated with leader channels due to the luminosity pulses propagating back along the channels once the SpcLs attach to the PELC. Of course, our ability to detect and track SpcL propagation was limited by our UHS camera pixel resolution and interframe interval (as discussed in Section 3.1). Also, note that for SpcLs that did not attach to their PELC, the inception-to-attachment-point length, time-to-attachment, and retrograde propagation speed, were not measurable as they did not have an attachment point on the PELC (either to its tip or lateral surface).

We calculated the percent increase in the AM downward leader propagation speeds for the two lowest altitude points in Figure 12 relative to the preceding higher altitude points for strokes in the 10 – 60 kA peak current range; the AM downward leader speed increased by 14% between the median altitude ranges of 183 and 155 m and by 52% between the median altitude ranges of 155 and 102 m. The leader acceleration is apparent at higher altitudes for strokes in our highest peak current range (84 – 228 kA); for strokes in this range, the AM (not shown in Figure 12) downward leader speed increased by 107% between the median altitude ranges of 1006 and 255 m. These findings are in agreement with modeled and observed increases in downward leader propagation speed a few hundred meters above ground assumed or reported in previous studies (Nag and Rakov, 2016; Cooray and Arevalo, 2017; Cruz et al., 2025). Cruz et al. (2025) analyzed 2-D speeds of 107 stepped leaders observed using high-speed video cameras in Utah and reported that for 91% of their stepped leaders the average propagation speed increased as they approached ground and that the average increase in speed was 69% at altitudes below 500 m AGL. Their observations of stepped leader acceleration close to ground in Utah (Southwestern United States) are generally consistent with ours in Florida (Southeasten United States).

On average, SpcL retrograde propagation speed and downward leader speed were faster for higher peak current strokes (see Figures 7 and 11, respectively). The median downward leader propagation speed (4.3×10^5 m/s) was about an order of magnitude slower than the median SpcL retrograde propagation speed of 4.0×10^6 m/s which is consistent with SpcL and leader-step formation

occuring at a signifantly faster rate in different branches of the downward leader resulting in the slower overall downward extension of the leader channel.

The SpcL inception-to-attachment-point length and retrograde propagation speed did not appear to be dependent upon the SpcL inception altitude. We found a weak correlation (R^2 = 0.20) between the SpcL length and inception altitude for SpcLs in all 18 strokes combined. On the other hand, a moderate correlation (R^2 = 0.68) was found between the length and the return stroke peak current. Also, the SpcL propagation speed appeared to be somewhat better correlated to the return stroke peak current (R^2 = 0.52) than the SpcL inception altitude (R^2 = 0.44). In order to further investigate the dependence of SpcL length and propagation speed on inception altitude, we repeated the analyses in Figures 8c and 9c, respectively, for each individual stroke. For SpcL length versus inception altitude, the R^2 values were less than 0.5 for all but two strokes for which they were 0.87 (N = 5) and 0.7 (N = 21). For SpcL propagation speed versus inception altitude, the maximum R^2 value was 0.31. So, for individual strokes, the overwhelming majority had weak correlations between the SpcL inception altitudes and their lengths/propagation speeds. The number of SpcLs observed and the altitude range of observations for each stroke were likely too small to effectively model the relationships between SpcL inception altitude and length/propagation speed. Additionally, we performed a random effects meta-analysis for individual strokes in our dataset for the same power-law relationships shown in Equations 1 and 2. The results of this analysis reinforced our findings that the SpcL length and propagation speed depend more on the return stroke peak current than the SpcL inception altitude. In addition, we found that the "random-effects" term in the analysis was significant, which could imply that stroke-to-stroke heterogeneity in factors such as unmeasured environmental conditions (see below) significantly influenced SpcL length and propagation speed. The return stroke peak current is correlated with the leader line charge density (Khounate et al., 2021; Kodali et al., 2005). Therefore, our findings indicate that SpcL characteristics are likely more influenced by the enhanced electric field in the immediate vicinity (within 10 meters or so) of the PELC than the ambient "background" electric field between the cloud and ground. We believe that the relationship between SpcL characteristics and their inception altitude to be more complicated due to the ambient electric field being dependent upon a variety of factors such as the specific thunderstorm, the lifecycle of the storm, the space charge environment closer to the ground, and the presence or absence of convection-driven charge movement. Note that we expect the surface fits in Figures 8a and 9a will become more robust as more data are recorded, especially for SpcLs at higher altitudes and for strokes with peak currents greater than 120 kA or so.

The VHF emissions associated with leader steps were observed to occur about 0.5 – 1 μs prior to the start of the predominantly low frequency (LF)-high frequency (HF) dE/dt leader step pulse (see Figure 10c-e). The VHF emissions are likely associated with the breakdown of virgin air and streamer formation occurring between the SpcL and the PELC, leading to the SpcL propagating toward the PELC prior to their attachment. The LF-HF dE/dt pulse is associated with current flow along longer (probably many tens of meters) sections of the PELC once the SpcL attaches to the PELC during the formation of a new leader step. The inception of the optical luminosity pulse, due to the heating associated with this current, occurs during the zero-crossing of the dE/dt pulse (i.e., the peak of the electric field pulse, see Figure 10b). The luminosity pulse then peaks within a few microseconds after its inception as the PELC continues to brighten due to continued current flow and channel heating. Thus, the luminosity pulse peak lags the radio frequency emissions, particularly the VHF emissions, which are likely associated with breakdown of air, streamer formation, followed by SpcL-PELC attachment. It remains to be seen if sources of the VHF emissions are predominantly located at the tip of the negatively charged PELC, the positive end of the SpcL, or both. Finally, as stated in Section 3.3, at least a portion of the delay of the optical pulse peaks relative to the LF-HF electric field pulse peaks could be due to the slower sampling rate (video camera interframe interval) of the mean gray level waveform.

For intracloud lightning negative leader propagation, Edens et al. (2014) measured a step length for a negative cloud-to-air leader from a color photograph as 200 m. Using a low-frequency lightning locating system, Wu et al. (2015) observed preliminary breakdown processes occurring in 662 intracloud lightning flashes. They found initial leader step lengths ranging from 40 to 140 m with an average step length and leader speed of 113 m and 4 x 10^5 m/s, respectively. Hare et al. (2020) used the Low Frequency Array (LOFAR) to observe an intracloud lightning discharge initiated at an altitude of 4 km with negative leaders spanning distances of 5 km. They found that each leader step emitted multiple short-duration (< 10 μs) bursts of radiation in their VHF observation band of 30 – 80 MHz and reported the median horizontal distance between VHF bursts to be 8.5 m. Pu and Cummer (2024) analyzed the initial development of intracloud lightning flashes using a 30 – 250 MHz broadband VHF interferometer. They observed structures at the corona fan edges which they suspected to be space stems. During intracloud lightning initial breakdown pulses and stepping, they observed discrete strong VHF pulses for over 50 μs scattered across a 100 – 200 m long linear structure. While our video camera measured downward CG leader median speed of 4.3 x 10^5 m/s is similar to that reported by Wu et al. (2015) for intracloud lightning, generally speaking, the step lengths (SpcL inception-to-attachment point lengths) observed by us in the visible frequency range for CG lightning are shorter than most stepping-associated

features observed in VHF for intracloud lightning. More observations and analyses are needed to understand the exact relationship between leader-step VHF emissions and the features of video-camera observed SpcLs as well as how stepping-associated emissions may differ for intracloud versus CG lightning leaders.

The retrograde propagation of the SpcL toward the negatively charged PELC is presumably occurring via breakdown of air at its positively charged end. Interestingly, the fastest optically-observed SpcL propagation speed in our dataset was 2.55 x 10^7 m/s, which is comparable to the speed (on the order of 10^7 m/s) of propagation of VHF sources reported for the so-called fast positive breakdown in cloud lightning (e.g., Rison et al., 2016; Lyu et al., 2019; Pu and Cummer, 2004; Shao et al., 2025). However, the vast majority of the SpcL propagation speeds in our dataset are on the order of 10^6 m/s (median = 4.0 x 10^6 m/s). We note that, Jensen and Shao (2025) used the 3-Dimensional Broadband Interferometric Mapping and Polarization system (BIMAP) to report fast positive breakdown VHF-source speeds in the roughly 1-20 x 10^6 m/s range in about 100 flashes, with the vast majority of the speeds being in the <10^7 m/s range (the median value was likely around 5 x 10^6 m/s). These speeds are also consistent with that obtained from the VHF observations of Sterpka et al. (2021) who interpreted the first in-cloud VHF sources in a flash reported by LOFAR as positive streamer activity propagating at a speed of 4.8 x 10^6 m/s. Jensen and Shao (2025) concluded that fast positive breakdown speeds on the order of >10^7 m/s should perhaps be considered as being at the extreme end of the speed distribution, which also agrees with our optically observed SpcL speed distribution. So, at least from the perspective of speed, our optical observations of the propagation of the positive end of SpcLs are similar to those for fast positive breakdown VHF-source propagation. The fast positive breakdown in cloud lightning reported in the scientific literature (see above) occur at higher altitudes (in-cloud) over lengths of about a hundred to several hundred meters and have durations of a few to few hundred microseconds, whereas our SpcLs in CG lightning negative stepped leaders have been observed closer to ground (below 1500 m AGL) and propagate over a few to few tens of meters during about 1 – 10 μs. Nonetheless, these Spcls seem to be another example of preferential positive breakdown followed by leader propagation.

5. Summary

We measured the characteristics of 364 SpcLs (326 of which attached to a PELC) in 18 negative CG strokes recorded using UHS video cameras at our MLO and KSC IAT measurement stations. The

median SpcL inception-to-attachment-point length and retrograde propagation speed were 8.2 m and 4.0 x 10^6 m/s, respectively. SpcL characteristics appear to be primarily dependent upon return-stroke peak current and weakly dependent upon the inception altitude. This is likely due to the relative proximity of the SpcL inception point to the PELC, which makes the electric field produced by the PELC line charge density one of the primary factors in determining SpcL characteristics. We observed that VHF emissions preceded the predominantly LF-HF dE/dt (or electric field) step pulse by around 0.5 – 1 μs and the visible-frequency-range luminosity pulses started during the dE/dt step pulses. The VHF emissions are likely associated with the breakdown of virgin air and streamer formation occurring between the SpcL and the PELC, leading to the SpcL propagating toward the PELC prior to their attachment. The LF-HF dE/dt pulse is associated with current flow along longer (probably many tens of meters) sections of the PELC once the SpcL attaches to the PELC during the formation of a new leader step. The optical luminosity pulse occurs due to the heating associated with this current. The median downward negative leader propagation speed for all strokes was 4.3 x 10^5 m/s, approximately one order of magnitude slower than the median SpcL retrograde propagation speed. Similar to SpcL retrograde propagation speeds, downward leader propagation speeds were generally faster for return strokes with higher peak currents. Also, on average, downward leader speeds increased as they progressed below a few hundred meters AGL. For strokes in the 10 – 60 kA peak current range, the AM downward leader speed increased by 14% between the median altitude ranges of 183 and 155 m and by 52% between the median altitude ranges of 155 and 102 m. For strokes in the 84 – 228 kA peak current range, the AM downward leader speed increased by 107% between the median altitude ranges of 1006 and 255 m.

Acknowledgments

The authors acknowledge funding from the U.S. National Science Foundation Award 1934066. The authors would like to thank Vaisala Inc. for providing the U.S. NLDN data. The data from the MLO and the KSC IAT are available by contacting A. Nag (anag@fit.edu).

References

Biagi, C. J., Jordan, D. M., Uman, M. A., Hill, J. D., Beasley, W. H., & Howard, J. (2009). High-speed video observations of rocket-and-wire initiated lightning. Geophysical Research Letters, 36(15). https://doi.org/10.1029/2009GL038525

Biagi, C. J., Uman, M. A., Hill, J. D., & Jordan, D. M. (2014). Negative leader step mechanisms observed in altitude triggered lightning. Journal of Geophysical Research: Atmospheres, 119(13), 8160–8168. https://doi.org/10.1002/2013JD020281

Biagi, C. J., Uman, M. A., Hill, J. D., Jordan, D. M., Rakov, V. A., & Dwyer, J. (2010). Observations of stepping mechanisms in a rocket-and-wire triggered lightning flash. Journal of Geophysical Research: Atmospheres, 115(D23). https://doi.org/10.1029/2010JD014616

Cooray, V., & Arevalo, L. (2017). Modeling the Stepping Process of Negative Lightning Stepped Leaders. Atmosphere, 8(12), 245. https://doi.org/10.3390/atmos8120245

Cruz, I. T., Saba, M. M. F., Silva, J. C. O., Abbasi, R. U., Hunt, H. G. P., Schumann, C., da Silva, D. R. R., da Silva, T. P., Lauria, P. B., & Kieu, N. T. (2025). Correlation between speed of the leader and peak current of the return stroke in negative lightning flashes. Geophysical Research Letters, 52(2), e2024GL111594. https://doi.org/10.1029/2024GL111594

Edens, H. E., Eack, K. B., Rison, W., & Hunyady, S. J. (2014). Photographic observations of streamers and steps in a cloud-to-air negative leader. Geophysical Research Letters, 41(4), 1336–1342. https://doi.org/10.1002/2013GL059180

Gao, Y., Lu, W., Ma, Y., Chen, L., Zhang, Y., Yan, X., & Zhang, Y. (2014). Three-dimensional propagation characteristics of the upward connecting leaders in six negative tall-object flashes in Guangzhou. Atmospheric Research, 149, 193–203. https://doi.org/10.1016/j.atmosres.2014.06.008

Goldberg, D., Nag, A., Plaisir, M., Cummins, K., Tempert, A., Brower, A., Biagi, C., & Rassoul, H. (2024). Optical and electric field signatures of space-leader evolution in negative cloud-to-ground lightning stepped leaders. International Conference on Lightning Protection, Germany, September 2024.

Hare, B. M., Scholten, O., Dwyer, J., Ebert, U., Nijdam, S., Bonardi, A., Buitink, S., Corstanje, A., Falcke, H., Huege, T., Hörandel, J. R., Krampah, G. K., Mitra, P., Mulrey, K., Neijzen, B., Nelles, A., Pandya, H., Rachen, J. P., Rossetto, L., … Winchen, T. (2020). Radio emission reveals inner meter-scale structure of negative lightning leader steps. Physical Review Letters, 124(10), 105101. https://doi.org/10.1103/PhysRevLett.124.105101

Hill, J. D., Uman, M. A., & Jordan, D. M. (2011). High-speed video observations of a lightning stepped leader. Journal of Geophysical Research: Atmospheres, 116(D16). https://doi.org/10.1029/2011JD015818

Idone, V. P., Orville, R. E., Hubert, P., Barret, L., & Eybert-Berard, A. (1984). Correlated observations of three triggered lightning flashes. Journal of Geophysical Research: Atmospheres, 89(D1), 1385–1394. https://doi.org/10.1029/JD089iD01p01385

Jensen, D. & Shao, X.-M. (2025), Fast initial discharge observations with BIMAP-3D, Atmospheric Discharges in Dynamic Environments Workshop, University of Bath, Bath, UK, 26 June 2025.

Jiang, R., Qie, X., Zhang, H., Liu, M., Sun, Z., Lu, G., Wang, Z., & Wang, Y. (2017). Channel branching and zigzagging in negative cloud-to-ground lightning. Scientific Reports, 7(1), 3457. https://doi.org/10.1038/s41598-017-03686-w

Khounate, H., Nag, A., Plaisir, M. N., Imam, A. Y., Biagi, C. J., & Rassoul, H. K. (2021). Insights on space-leader characteristics and evolution in natural negative cloud-to-ground lightning. Geophysical Research Letters, 48(16). https://doi.org/10.1029/2021GL093614

Kodali, V., Rakov, V. A., Uman, M. A., Rambo, K. J., Schnetzer, G. H., Schoene, J., & Jerauld, J. (2005). Triggered-lightning properties inferred from measured currents and very close electric fields. Atmospheric Research, 76, 355–376. https://doi.org/10.1016/j.atmosres.2004.11.036

Lyu, F., Cummer, S. A., Qin, Z., & Chen, M. (2019). Lightning initiation processes imaged with very high frequency broadband interferometry. Journal of Geophysical Research: Atmospheres, 124(6), 2994–3004. https://doi.org/10.1029/2018JD029817

Nag, A., Cummins, K. L., Plaisir, M. N., Wilson, J. G., Crawford, D. E., Brown, R. G., Noggle, R. C., & Rassoul, H. K. (2021). Inferences on upward leader characteristics from measured currents. Atmospheric Research, 251, 105420. https://doi.org/10.1016/j.atmosres.2020.105420

Nag, A., Cummins, K.L., Plaisir, M.N., Brown, R.G., Wilson, J.G., Crawford, D.E., Noggle, R.C., Rassoul, H.K., (2023a). Characteristics of upward-connecting-leader current leading to attachment in downward negative cloud-to-ground lightning strokes. Atmospheric Research, 294, 106943. https://doi.org/10.1016/j.atmosres.2023.106943.

Nag, A., Khounate, H., Cummins, K. L., Goldberg, D. J., Imam, A. Y., Plaisir, M. N., & Rassoul, H. K. (2023b). Parameters of the lightning attachment processes in a negative cloud-to-ground stroke observed on a microsecond timescale. Geophysical Research Letters, 50, e2023GL104196. https://doi.org/10.1029/2023GL104196

Nag, A., & Rakov, V. A. (2016). A unified engineering model of the first stroke in downward negative lightning. Journal of Geophysical Research: Atmospheres, 121(5), 2188–2204. https://doi.org/10.1002/2015JD023777

Petersen, D. A., & Beasley, W. H. (2013). High-speed video observations of a natural negative stepped leader and subsequent dart-stepped leader. Journal of Geophysical Research: Atmospheres, 118(21), 12,110-12,119. https://doi.org/10.1002/2013JD019910

Plaisir, M., Nag, A., Cummins, K., Goldberg, D., Biagi, C., Brown, R., & Rassoul, H. K., (2023). The lightning attachment processes observed on a submicrosecond-scale: Measurements of current and video. International Conference on Grounding & Lightning Physics and Effects Belo Horizonte, Brazil, May 2023.

Pu, Y., & Cummer, S. A. (2024). Imaging step formation in in-cloud lightning initial development with VHF interferometry. Geophysical Research Letters, 51(1), e2023GL107388. https://doi.org/10.1029/2023GL107388

Qi, Q., Lu, W., Ma, Y., Chen, L., Zhang, Y., & Rakov, V. A. (2016). High-speed video observations of the fine structure of a natural negative stepped leader at close distance. Atmospheric Research, 178–179, 260–267. https://doi.org/10.1016/j.atmosres.2016.03.027

Qi, Q., Lyu, W., Ma, Y., Wu, B., Chen, L., Jiang, R., Zhu, Y., & Rakov, V. A. (2019). High-speed video observations of natural lightning attachment process with framing rates up to half a million frames per second. Geophysical Research Letters, 46(21), 12580–12587. https://doi.org/10.1029/2019GL085072

Rison, W., Krehbiel, P. R., Stock, M. G., Edens, H. E., Shao, X.-M., Thomas, R. J., Stanley, M. A., & Zhang, Y. (2016). Observations of narrow bipolar events reveal how lightning is initiated in thunderstorms. Nature Communications, 7(1), 10721. https://doi.org/10.1038/ncomms10721

Shao, X.-M., Jensen, D. P., Ho, C., Caffrey, M. P., Raby, E. Y., Graham, P. S., Haynes, W. B., & Blaine, W. G. (2025). 3D Radio frequency mapping and polarization observations show lightning flashes were ignited by cosmic-ray showers. Journal of Geophysical Research: Atmospheres, 130(5), e2024JD042549. https://doi.org/10.1029/2024JD042549

Srivastava, A., Jiang, R., Yuan, S., Qie, X., Wang, D., Zhang, H., Sun, Z., & Liu, M. (2019). Intermittent propagation of upward positive leader connecting a downward negative leader in a negative cloud-to-ground lightning. Journal of Geophysical Research: Atmospheres, 124(24), 13763–13776. https://doi.org/10.1029/2019JD031148

Sterpka, C., Dwyer, J., Liu, N., Hare, B. M., Scholten, O., Buitink, S., Veen, S. ter, & Nelles, A. (2021). The spontaneous nature of lightning initiation revealed. Geophysical Research Letters, 48(23), e2021GL095511. https://doi.org/10.1029/2021GL095511

Tran, M. D., Rakov, V. A., & Mallick, S. (2014). A negative cloud-to-ground flash showing a number of new and rarely observed features. Geophysical Research Letters, 41(18), 6523–6529. https://doi.org/10.1002/2014GL061169

Wu, T., Yoshida, S., Akiyama, Y., Stock, M., Ushio, T., & Kawasaki, Z. (2015). Preliminary breakdown of intracloud lightning: Initiation altitude, propagation speed, pulse train characteristics, and step length estimation. Journal of Geophysical Research: Atmospheres, 120(18), 9071–9086. https://doi.org/10.1002/2015JD023546

Author statement

Dylan J. Goldberg: data curation, formal analysis, investigation, methodology, validation, visualization, writing - original draft, writing - review & editing
Amitabh Nag: conceptualization, data curation, formal analysis, investigation, methodology, project administration, supervision, validation, writing - original draft, writing - review & editing
Kenneth L. Cummins: formal analysis, investigation, methodology, supervision, validation, writing - original draft, writing - review & editing
Mathieu N. Plaisir: data curation
Alex Tempert: data curation
A. Tyler Brower: data curation
Christopher J. Biagi: data curation
Robert G. Brown: data curation
Hamid K. Rassoul: project administration, supervision, writing - review & editing

Declaration of interests

The authors declare that they have no known competing financial interests or personal relationships that could have appeared to influence the work reported in this paper.

Highlights:

- Space-leader lengths and speeds increased with increasing return-stroke peak currents.

- Space-leader inception altitudes did not significantly impact their lengths.
- VHF emissions preceded electric field leader-step pulses.